

Micromechanically Based Poroelastic Modeling of Fluid Flow in Haversian Bone

C. C. Swan¹

Civil and Environmental Engineering,
University of Iowa,
Iowa City, IA 52242

R. S. Lakes

Engineering Physics,
University of Wisconsin-Madison

R. A. Brand

Orthopaedic Surgery,
University of Iowa,
Iowa City, IA 52242

K. J. Stewart

Civil & Environmental Engineering,
University of Iowa,
Iowa City, IA 52242

To explore the hypothesis that load-induced fluid flow in bone is a mechano-transduction mechanism in bone adaptation, unit cell micro-mechanical techniques are used to relate the microstructure of Haversian cortical bone to its effective poroelastic properties. Computational poroelastic models are then applied to compute in vitro Haversian fluid flows in a prismatic specimen of cortical bone during harmonic bending excitations over the frequency range of 10^0 to 10^6 Hz. At each frequency considered, the steady state harmonic response of the poroelastic bone specimen is computed using complex frequency-domain finite element analysis. At the higher frequencies considered, the breakdown of Poiseuille flow in Haversian canals is modeled by introduction of a complex fluid viscosity. Peak bone fluid pressures are found to increase linearly with loading frequency in proportion to peak bone stress up to frequencies of approximately 10 kHz. Haversian fluid shear stresses are found to increase linearly with excitation frequency and loading magnitude up until the breakdown of Poiseuille flow. $\tan \delta$ values associated with the energy dissipated by load-induced fluid flow are also compared with values measured experimentally in a concurrent broadband spectral analysis of bone. The computational models indicate that fluid shear stresses and fluid pressures in the Haversian system could, under physiologically realistic loading, easily reach the level of a few Pascals, which have been shown in other works to elicit cell responses in vitro. © 2003 American Institute of Physics. [DOI: 10.1115/1.1535191]

Keywords: Bone Adaptation, Fluid Flow, Mechano-Transduction, Poroelasticity, Homogenization, Unit Cell Analysis, Complex Finite Element Analysis

Introduction and Motivation

Bone adaptation is a well-recognized phenomenon in which human and/or animal bones slowly add or lose mass and alter their form in response to alterations in the normal mechanical history. Despite the fact that bone adaptation is a well-recognized phenomenon, the specific mechanical stimuli that trigger, sustain, and terminate bone adaptation are not presently well characterized or understood. Cyclic loading of bone over and above normal homeostatic stimulus clearly alters the microscale environment in which osteocytes (cells postulated to sense mechanical signals) reside [1,2]. While the macroscopic stress magnitudes and cyclic loading frequencies that do produce positive bone adaptation have been identified [3,4] the microscale stimuli to which osteocytes respond are not yet understood.

Over the past century or more, investigators have posed many mechanisms for the adaptive response of bone to mechanical stimuli. Perhaps the most well-known was that of Wolff, who postulated bones adapted to principal tensile and compressive stresses according to mathematical laws [5]. Many researchers through the first three-quarters of the 20th century presumed a direct mechanical stimulus (although often this was more implicit than explicit and did not necessarily exclude underlying mechanisms of various sorts) [6–15]. More recently, a number of investigators have proposed different chemical, electrical, and mechanical stimuli to osteocytes deriving from cyclic loading of bone. Some of these stimuli are associated with load-induced fluid flow in the different pore structures of cortical bone while others are

not. Yasuda (1954) [16] and Fukada and Yasuda (1957) [17] introduced the notion that piezoelectrical-phenomena exist in dry bone, and Bassett and Becker later hypothesized that piezoelectricity could play a role in bone remodeling [18]. Piekarski and Munro postulated a chemical mechanism based on the notion that load-induced fluid flow in bone enhances the rate of nutrient supply and waste removal to and from osteocytes, thereby providing a more favorable environment for production of additional bone mass [19]. The observation of strong electric potential gradients in the vicinity of Haversian canals of cortical bone undergoing different types of loading added support for electrical mechanisms [20,21]. Subsequently, investigators proposed that the nature of these electrical fields could be explained and attributed to fluid flow in the pores of the hydroxyapatite matrix [22,23] or flow in the larger canaliculi [24]. Alternatively, it has been proposed that shearing stresses from the oscillating flow of viscous bone fluids exert stimulatory stresses on the osteocytes or their processes [25,26]. Still further works have been aimed at determining whether or not the fluid pressures in bone fluids during physiological dynamic loadings can possibly serve as the stimulus to which osteocytes respond [27,28].

To test these hypotheses, we need realistic estimates of fluid flow to ascertain whether experimentally these levels of flow indeed appropriately stimulate bone cells. Since we cannot experimentally measure fluid flow at the necessary levels, realistic models at the microstructural level are needed. One approach is to create coherent and hierarchical multiple-scale poroelastic models for each of the known flow systems. The objective of the present work is therefore to establish the foundations of such a model, but confines the work to flow in the Haversian and Volkmann canals. (We intend to extend the computations at finer scales (e.g., canalicular systems) in the near future.)

A recent review of bone poroelasticity models by Cowin suggests that there are many free parameters in isotropic bone poro-

¹Corresponding author: Colby C. Swan; 4120 Seamans Center for Engineering Arts; Department of Civil and Environmental Engineering; The University of Iowa; Iowa 52242 USA; E-mail: colby-swan@uiowa.edu; Phone: 1(319) 335-5831; Fax: 1(319)335-5660.

Contributed by the Bioengineering Division for publication in the JOURNAL OF BIOMECHANICAL ENGINEERING. Manuscript received February 2002; revised manuscript received, September 2002. Associate Editor: J. D. Humphrey.

roelasticity models that must be selected by the analyst [29]. To some extent, difficult questions and uncertainties pertaining to selection of model parameters cannot be avoided. In this work, an attempt is made to capture the gross microstructural characteristics of Haversian bone and to couple this with unit cell microstructural analysis techniques. Together, these lead to a poroelastic model featuring transversely isotropic symmetry. Based on the assumed microstructure of Haversian bone [30], the effective bone poroelastic properties are determined. In the current work the lamellar structure of cortical bone matrix is neglected, and the bone matrix is modeled simply as a linear isotropic elastic (and homogeneous) solid. Similarly, the bone fluid is assumed to be a Newtonian fluid with a constant viscosity and bulk modulus. Despite these simplifying assumptions, the modeling framework developed and proposed here is general enough that more realistic behaviors can subsequently be incorporated.

In the remainder of this article, the basic microstructure and kinematics of bone matrix and vascular fluid in Haversian bone are considered. Microscale stresses and strains on the osteonal scale are related to macroscopic stresses and strains on a larger bone specimen length scale (on the order of a centimeter). A linear poroelastic model is proposed to relate averaged microscale stresses to strains, and changes in fluid content. A unit-cell analysis procedure is used to estimate the coefficients of this poroelastic model for specific physical characteristics of the bone. FEM implementation of the poroelastic bone model is then presented, and complex, frequency-domain, poroelastic modeling of cortical bone specimens undergoing forced vibrations is then considered. The dissipated mechanical energy in these vibrations is computed for comparison to experimental measurements made on human cortical bone specimens. The peak computed fluid pressures and shear stresses in the Haversian system are also presented and discussed. Finally, the limitations and assumptions of the model are discussed, along with their possible impact on the computed results.

Unit Cell Analysis of Haversian Bone

Length Scales and Averaging Domains. Haversian bone (Fig. 1) is formed by arrays of osteons, each having a lamellar bone matrix structure, and a Haversian canal running along the approximate central axis. As a first approximation, Haversian bone can be modeled as a linear, isotropic, elastic medium through which a periodic array of fluid-filled Haversian canals pass (Fig. 2)². A macroscopic bone specimen under consideration will occupy a domain Ω_B in three-dimensional space and can, for simplicity, be idealized as exhibiting a periodic microstructure in that the specimen is formed by continuous repetition of the unit cell $\Omega_s = \prod_{i=1}^3]0, \lambda_i[$, where λ_i are the dimensions of the cell. Physically for Haversian bone, the unit cell would be the material structure associated with an osteon as shown in Fig. 1. Two distinct length scales will be considered in the present analysis: the bone specimen length scale ($\ell \approx 1-10$ cm) and the Haversian/osteonal micro-scale $\lambda \approx 100$ μ m.

A material point in an undeformed unit cell Ω_s is specified by its local microscale material coordinates \mathbf{X} , while the same point in the deformed unit cell is located by its spatial microscale coordinates \mathbf{x} . Similarly, on the bone specimen length scale, the Lagrangian and spatial macroscale coordinates of a reference point in Ω_B are denoted, respectively, by \mathbf{Y} and \mathbf{y} . On both micro and bone specimen scales, displacement vectors relate reference points in the undeformed state to those in the deformed state:

$$\mathbf{x} = \mathbf{X} + \mathbf{u}(\mathbf{X}) \quad \text{microscale}; \quad (1a)$$

$$\mathbf{y} = \mathbf{Y} + \mathbf{u}(\mathbf{Y}) \quad \text{macroscale}. \quad (1b)$$

²The study of Cooper et al. (1966) [30] on canine femur specimens indicates that Haversian canals are in reality approximately 50% filled with endothelial cells and osteoblasts. The effects of these soft tissues in the Haversian canals are neglected in this analysis, although they are discussed subsequently.

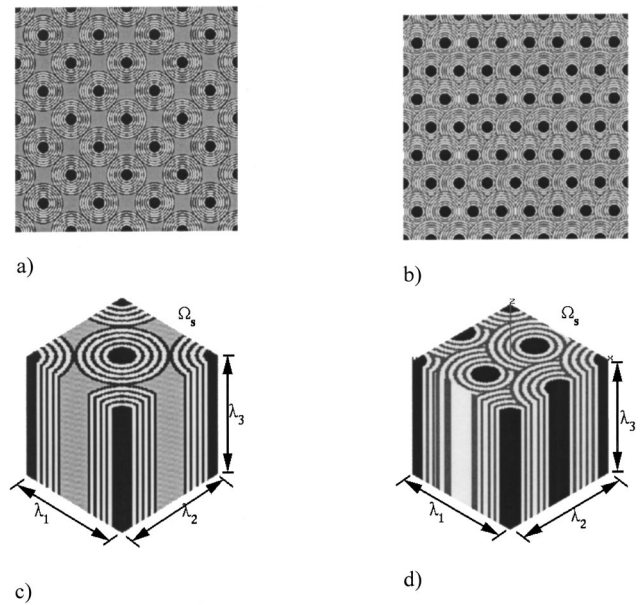


Fig. 1 Three-dimensional idealizations of Haversian bone. a) transverse section with square-packed non-overlapping osteons; b) transverse section with hexagonally packed, overlapping osteons; c) unit cell for non-overlapping osteons; d) unit cell for overlapping osteons.

In the following, the microscale coordinates \mathbf{X} are employed in solving unit cell analysis problem to find the effective property-structure relations of Haversian bone, while the macroscale coordinates \mathbf{Y} are used in structural analysis of macroscopic bone specimens with dimensions $O(\ell)$ much larger than those of the Haversian/osteonal unit cell. In structural analysis of bone specimens, the effective poroelastic properties of Haversian bone are employed.

Haversian bone is considered to be fully saturated, having only a solid bone-matrix phase and a fluid phase with no air voids. The respective volume fractions of both fluid and solid phases in a typical unit cell Ω_s are represented as follows:

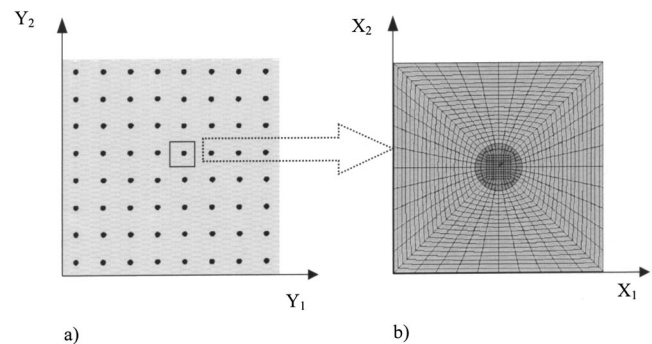


Fig. 2 a) Idealized transverse section through Haversian bone with lamellar structure neglected and bone matrix treated as linear, isotropic, homogeneous elastic medium; b) finite element mesh of unit cell model with 4% Haversian porosity. To estimate poroelastic model coefficients, five strain-controlled tests were performed on this model: (1) undrained $\bar{\epsilon}_{11} \neq 0$; (2) undrained $\bar{\epsilon}_{33} \neq 0$; (3) undrained $\bar{\gamma}_{12} \neq 0$; (4) undrained $\bar{\gamma}_{13} \neq 0$; and (5) drained $\bar{\epsilon}_{11} \neq 0$.

$$\varphi_{\text{solid}} = \frac{V_{\text{solid}}}{V_{\text{solid}} + V_{\text{fluid}}}; \quad \varphi_{\text{fluid}} = \frac{V_{\text{fluid}}}{V_{\text{solid}} + V_{\text{fluid}}} \quad (2)$$

where φ_{solid} and φ_{fluid} sum to unity.

Microscale and Macroscale Bone Kinematics. On the domain of the unit cell Ω_s , the micro-scale displacement field in the bone matrix is denoted by $\mathbf{u}^s(\mathbf{X})$, $\forall \mathbf{X} \in \Omega_s^{\text{solid}}$ and similarly the micro-scale displacement field in the Haversian fluid by $\mathbf{u}^f(\mathbf{X})$, $\forall \mathbf{X} \in \Omega_s^{\text{fluid}}$. The micro-scale averages of the solid and fluid velocity fields over their respective portions of Ω_s are computed:

$$\bar{\mathbf{v}}^s = \frac{1}{V_{\text{solid}}} \int_{\Omega_s^{\text{solid}}} \mathbf{v}^s(\mathbf{X}) d\Omega_s^{\text{solid}}; \quad \bar{\mathbf{v}}^f = \frac{1}{V_{\text{fluid}}} \int_{\Omega_s^{\text{fluid}}} \mathbf{v}^f(\mathbf{X}) d\Omega_s^{\text{fluid}}; \quad (3)$$

The total volume-averaged velocity on the micro-scale provides what is called the *total velocity* of the medium:

$$\bar{\mathbf{v}}(\mathbf{Y}) = \phi_{\text{solid}} \bar{\mathbf{v}}^s + \phi_{\text{fluid}} \bar{\mathbf{v}}^f \quad (4)$$

This expression can be rewritten in a more useful form as follows:

$$\bar{\mathbf{v}}(\mathbf{Y}) = \bar{\mathbf{v}}^s + \dot{\mathbf{w}} \quad (5)$$

in which

$$\dot{\mathbf{w}} = \phi_{\text{fluid}} (\bar{\mathbf{v}}^f - \bar{\mathbf{v}}^s). \quad (6)$$

Written this way, the average velocity of the medium has two components: the average velocity of the bone matrix $\bar{\mathbf{v}}^s$ and the so-called *discharge velocity* $\dot{\mathbf{w}}$ which represents the average relative velocity between the fluid and the bulk medium per unit gross cross-sectional area, and is an indicator of instantaneous fluid flow in the bone.

It can be shown that the net rate of volumetric fluid flow per gross unit volume into a local region about a macroscopic point \mathbf{Y} represents a rate of change in volumetric fluid-content which is denoted by $\dot{\zeta}$ and is available from the both the microscale flux and the macro-scale divergence of $\dot{\mathbf{w}}$:

$$\dot{\zeta} = \frac{-1}{V} \int_{\Gamma_{\text{fluid}}} \mathbf{n} \cdot (\mathbf{v}^f - \bar{\mathbf{v}}^s) d\Gamma_{\text{fluid}} \quad (7a)$$

$$= -\nabla_{\mathbf{Y}} \cdot \dot{\mathbf{w}} \quad (7b)$$

$$= -\frac{\partial \dot{w}_i}{\partial Y_i}. \quad (7c)$$

Under ‘‘very rapid’’ loadings applied to Haversian bone, there is insufficient time for the fluid in the canals to overcome the viscous and inertial forces that resist flow, and thus $\dot{\mathbf{w}} = \mathbf{0}$. Conversely, under loadings applied relatively slowly or with sufficiently ‘‘long duration,’’ there is ample time for the fluid to overcome viscous and inertial forces that resist flow. However, once excess fluid pressures have been relieved, flow ceases once again, such that $\dot{\mathbf{w}} = \mathbf{0}$. The response of bone during rapid loading in which no flow occurs is termed *undrained*, whereas the response of bone in which the fluid carries no excess pressures from applied loadings, is termed *fully drained*. These two cases provide limits between which bone features a response that is partially drained with fluid flow and pressure relaxation occurring.

Microscale and Macroscale Stresses and Strains. The macroscopic strain rate in the bone matrix can be related to the microscale strain rate field and the macro-scale velocity field as follows:

$$\dot{\boldsymbol{\epsilon}} = \frac{1}{V} \left[\int_{\Omega_{\text{solid}}} \dot{\boldsymbol{\epsilon}}^s d\Omega_{\text{solid}} + \int_{\Gamma_{\text{fluid-solid}}} \frac{1}{2} (\mathbf{n} \otimes \mathbf{v}^s + \mathbf{v}^s \otimes \mathbf{n}) d\Gamma_{\text{fluid-solid}} \right] \quad (8a)$$

$$= \varphi_{\text{solid}} \dot{\boldsymbol{\epsilon}}^s + \varphi_{\text{voids}} \dot{\boldsymbol{\epsilon}}^{\text{voids}} \quad (8b)$$

$$= \frac{1}{2} (\nabla_{\mathbf{Y}} \bar{\mathbf{v}}^s + \bar{\mathbf{v}}^s \nabla_{\mathbf{Y}}) \quad (8c)$$

In (8a) \mathbf{n} represents the unit outward normal vector from the edges of Haversian canals, directed into the bone matrix.

Macroscopic stresses $\bar{\boldsymbol{\sigma}}(\mathbf{Y})$ in Haversian bone are simply spatial averages of the microscale stress $\boldsymbol{\sigma}(\mathbf{X})$, which can fluctuate quite significantly within Ω_s due to material heterogeneity. When referring to macroscopic stresses, there are at least three possibilities for describing their apportionment between the fluid and solid phases: the total average stress in the medium at a point \mathbf{Y} denoted $\bar{\boldsymbol{\sigma}}(\mathbf{Y})$; the average stress in the solid bone matrix $\bar{\boldsymbol{\sigma}}^s(\mathbf{Y})$; and the average stress in the fluid $\bar{\boldsymbol{\sigma}}^f(\mathbf{Y})$. Mathematically, the average stresses in the matrix and fluid phases are, respectively:

$$\bar{\boldsymbol{\sigma}}^s = \frac{1}{V_{\text{solid}}} \int_{\Omega_{\text{solid}}} \boldsymbol{\sigma}^s(\mathbf{X}) d\Omega_{\text{solid}}; \quad \bar{\boldsymbol{\sigma}}^f = \frac{1}{V_{\text{fluid}}} \int_{\Omega_{\text{fluid}}} \boldsymbol{\sigma}^f(\mathbf{X}) d\Omega_{\text{fluid}}; \quad (9)$$

The average fluid pressure \bar{p}^f is related to the averaged fluid stress tensor as:

$$\bar{p}^f = -\frac{1}{3} \text{tr}(\bar{\boldsymbol{\sigma}}^f) \quad (10)$$

The total average stresses at a point \mathbf{Y} in Haversian bone are the volume-weighted sum of the stresses in the fluid and solid phases

$$\bar{\boldsymbol{\sigma}} = \varphi_{\text{solid}} \bar{\boldsymbol{\sigma}}^s + \varphi_{\text{fluid}} \bar{\boldsymbol{\sigma}}^f \quad (11)$$

which shows that any two of the three average stresses uniquely determine the third.

A PoroElastic Constitutive Model. On the length scale of a few centimeters, Haversian bone can for most physiological loadings be modeled as a linearly elastic poroelastic continuum whose average stresses, strains and change in fluid content are related by a Biot-type constitutive model [31,32]. The state of average stress in the bone specimen about a macroscopic point \mathbf{Y} can be quantified by the components of the symmetric averaged stress tensor defined in (11), and the state of average deformation in the medium by the six components of the averaged strain tensor defined in (8):

$$\bar{\boldsymbol{\sigma}} = [\bar{\sigma}_{11} \quad \bar{\sigma}_{22} \quad \bar{\sigma}_{33} \quad \bar{\sigma}_{23} \quad \bar{\sigma}_{31} \quad \bar{\sigma}_{12}] \quad (12a)$$

$$\bar{\boldsymbol{\epsilon}} = [\bar{\epsilon}_{11} \quad \bar{\epsilon}_{22} \quad \bar{\epsilon}_{33} \quad \bar{\gamma}_{23} \quad \bar{\gamma}_{31} \quad \bar{\gamma}_{12}] \quad (12b)$$

The locally averaged fluid pressure in the medium in the neighborhood of a macroscale point \mathbf{Y} is quantified by \bar{p}^f , and the change in fluid content in that same neighborhood by ζ . The seven macroscopic stress variables can be related to the seven macroscopic strain and flow variables through the linear mathematical relationship below, a variation of which was originally proposed by Biot (1941) [31]:

$$\begin{bmatrix} \bar{\boldsymbol{\sigma}} \\ \bar{p}^f \end{bmatrix} = \begin{bmatrix} \mathbf{C} & \mathbf{G} \\ \mathbf{G}^T & Z \end{bmatrix} \cdot \begin{bmatrix} \bar{\boldsymbol{\epsilon}} \\ \zeta \end{bmatrix} \quad (13)$$

in which, the terms of \mathbf{C} , a symmetric 6×6 matrix, comprise the undrained poroelastic stiffness tensor of fluid-filled bone, and \mathbf{G} , a 6×1 matrix, captures the coupling between change in fluid content and change in total stress, and Z , a scalar, is the *storage modulus* that denotes the coupling between change in fluid pressure and change in fluid content with strain held fixed. These moduli are generally dependent upon the stiffness properties of the bone matrix and those of the bone fluid, and also their respective microstructural arrangements. An inverse expression of the same poroelasticity model is

$$\begin{bmatrix} \bar{\boldsymbol{\epsilon}} \\ \zeta \end{bmatrix} = \begin{bmatrix} \mathbf{S} & \mathbf{B} \\ \mathbf{B}^T & A \end{bmatrix} \cdot \begin{bmatrix} \bar{\boldsymbol{\sigma}} \\ \bar{p}^f \end{bmatrix} \quad (14)$$

In the preceding expression, \mathbf{S} is the fully-drained compliance of the bone-matrix, taking into account the orientation and magnitude of the Haversian porosity; \mathbf{B} relates changes in average fluid pressure to average matrix strains; and \mathbf{A} is the storage compliance of the medium. Generally for Haversian bone, the partitioned poroelastic stiffness and compliance operators would be expected to feature transverse isotropy, due to the quasi-random arrangement of Haversian canals and osteons within the cross-section of a long bone specimen.

Determination of Poroelastic Coefficients by Unit Cell Analysis. While techniques for experimental measurement of poroelasticity parameters for isotropic media were outlined decades ago [33] physical measurement of these moduli remains challenging even today. As a viable alternative, microscale unit cell analysis of the stresses and strains in the bone matrix and the Haversian fluid under both undrained and fully-drained conditions can be used to estimate the constants. This approach has the advantage that the properties of the bone matrix and the pore fluid as well as their microstructural arrangements can be related to the anisotropic effective poroelastic properties. Unit cell analysis is typically performed on composite materials having periodic micro-structures [34–36]. The essential idea is to take the unit cell, or the basic microstructural unit which repeats, and to perform computational experiments on it, while imposing periodic boundary conditions which force the unit cell to behave as if it were still embedded in the periodic medium from which it was extracted.

The poroelastic model coefficients of (13) can be determined by performing experiments on the unit cell in both completely *undrained* and completely *drained* modes. In the former, the bone matrix and the pore fluid move together ($\dot{\mathbf{w}}=\mathbf{0}$), and in the latter, only displacements in the solid bone matrix need to be considered ($\bar{\mathbf{p}}^f=0$). Due to the assumed periodicity of the bone's microstructure, deformation of the bone matrix on the osteonal scale satisfies a linear-periodic decomposition:

$$\mathbf{u}^s(\mathbf{X}, \mathbf{Y}) = \bar{\boldsymbol{\varepsilon}}(\mathbf{Y}) \cdot \mathbf{X} + \mathbf{u}_{\text{per}}^{*s}(\mathbf{X}) \quad (15)$$

where $\bar{\boldsymbol{\varepsilon}}$ is the macroscopic strain tensor defined in (8) and $\mathbf{u}_{\text{per}}^{*s}(\mathbf{X})$ is a purely periodic displacement field that repeats in all adjacent unit cells

In the undrained analysis, no fluid flow occurs, and the unit cell of Haversian bone, as modeled, behaves as a two-phased fluid-solid elastic composite. The objective of undrained unit cell analysis is to apply directional loadings to the unit cell, and to study the resulting apportionment of stresses and strains between the fluid and solid phases.

The generic strain-controlled homogenization problem involves imposing a displacement field $\mathbf{u}(\mathbf{X}) = \bar{\boldsymbol{\varepsilon}} \cdot \mathbf{X}$ associated with a prescribed macroscopic strain tensor $\bar{\boldsymbol{\varepsilon}}_{ij}$ on the unit cell. Due to the heterogeneity of materials and their properties, such a uniform strain field will not lead to a stress-field that satisfies local equilibrium conditions ($\sigma_{ij,j}=0$) on the microscale. The purely periodic contribution to the displacement field $\mathbf{u}_{\text{per}}^{*s}(\mathbf{X})$ must therefore be computed so as to satisfy stress-field equilibrium within the unit cell. Once the equilibrium microscale stress field $\boldsymbol{\sigma}(\mathbf{X})$ and strain field $\boldsymbol{\varepsilon}(\mathbf{X})$ are known, the corresponding macroscopic total stress tensor $\bar{\boldsymbol{\sigma}}^{(ij)}$ and the corresponding fluid pressure $\bar{p}^{(ij)}$ in response to the applied $\bar{\boldsymbol{\varepsilon}}_{ij}$ are computed following (9) and (10). Since under undrained loadings of the unit cell ζ necessarily vanishes, most of the poroelastic stiffness tensor components can be computed straightforwardly from the undrained analysis. Specifically, using the condensed notations of (12) and (13)

$$C_{ij} = \frac{\bar{\sigma}_i^{(j)}}{\bar{\varepsilon}_j} \quad i \in \{1, 2, \dots, 6\} \quad j \in \{1, 2, \dots, 6\}. \quad (16)$$

where, using condensed notation, $\bar{\sigma}_i^{(j)}$ is the resulting i^{th} macro-scale stress component in the medium due to application of the macroscopic j^{th} strain component. Similarly, the six coefficients of \mathbf{G} can be determined as follows:

$$G_j = \frac{\bar{p}^{f(j)}}{\bar{\varepsilon}_j} \quad j \in \{1, 2, \dots, 6\} \quad (17)$$

where $\bar{p}^{f(j)}$ is the averaged fluid pressure due to application of the j^{th} strain component.

The storage modulus Z is most easily computed using a fully-drained analysis of the unit cell that can be replicated by modeling the Haversian canals as devoid of fluid. In this case, under any applied loading it will be true that $\bar{p}^f=0$. Applying any single strain-controlled loading to the unit cell with a non-vanishing volumetric component yields the value of Z as:

$$Z = - \frac{G_j \bar{\varepsilon}_j}{\zeta}, \quad \text{no summation on } j, \quad \text{and } j \in \{1, 2, \dots, 6\} \quad (18)$$

where ζ here is simply the averaged volume strain associated with the fluid cavity, computed for the special case of fully drained loading from (8b) as:

$$\zeta = \text{tr}(\bar{\boldsymbol{\varepsilon}}) - \varphi_{\text{solid}} \text{tr}(\bar{\boldsymbol{\varepsilon}}^s). \quad (19)$$

Based on the assumed periodic arrangement of Haversian canals shown in Fig. 2, the computed poroelastic stiffness coefficients feature square, orthotropic symmetry. Though not a part of this work, the computed orthotropic poroelasticity tensor can be converted to a transversely isotropic one by performing an orientational average of the stiffness coefficients in the transverse X_1 - X_2 plane.

Effective Fluid-Conductivity Properties. The relation between average fluid velocities (6) and average fluid pressure gradients (10) in Haversian bone is governed by Darcy's Law:

$$\dot{w}_i = -k_{ij} h_{,j} \quad (20)$$

where the terms k_{ij} comprise the effective permeability tensor of Haversian bone, and $h = \bar{p}^f - \rho^f(\mathbf{Y} \cdot \mathbf{b})$ is the piezometric pressure in the medium, where ρ^f is the mass density of the bone fluid and \mathbf{b} provides the direction and magnitude of gravitational acceleration acting on the medium. In (20) the spatial derivatives of h [i.e., $h_{,j}$] are computed on the macroscopic scale as opposed to the microscale.

The permeability of Haversian bone can be related to the microstructure by making the assumption of uni-directional flow in the canals. Assuming that there is a harmonically oscillating macroscopic pressure gradient driving oscillatory flow in a given canal, conservation of fluid mass, and the assumption of an incompressible fluid lead to the following governing differential equation for flow in the canal:

$$r^2 v_f'' + r v_f' - \frac{i \omega \rho^f}{\mu} r^2 v_f = \frac{r^2 h_{,x}}{\mu} \quad (21)$$

where $v_f(r,t)$ is the fluid velocity distribution in the canal, r is the radial coordinate measured from the center of the canal, x is the coordinate variable along the canal's axis, ρ^f is the fluid density, ω is the angular frequency of excitation, and μ is the viscosity of the fluid. Biot [32] has shown that the solution to this equation is

$$v_f(r,t) = \frac{i h_{,x}}{\rho^f \omega} \left[\frac{I_0\left(\frac{i^{1/2} r}{\beta}\right)}{I_0\left(\frac{i^{1/2} R}{\beta}\right)} - 1 \right] \exp(i \omega t) \quad (22)$$

where R is the radius of the cylindrical canal and $\beta = [\mu/(\rho^f \omega)]^{1/2}$ is the approximate thickness of the viscous boundary layer. Taking the average of the fluid velocity over the canal's cross-section provides the so-called *seepage velocity* as follows

$$\bar{v}_i(t) = \frac{i h_{xx}}{\rho^f \omega} \left[-i + 2\kappa \frac{I_1(i^{1/2}\kappa)}{I_0(i^{1/2}\kappa)} \right] \exp(i\omega t) \quad (23)$$

where $\kappa = R/\beta = R[\mu/(\rho^f \omega)]^{-1/2}$. Now, letting $\bar{v}_i = \dot{w}_i / \phi_{\text{fluid}}$, the effective permeability of the bone in the direction of the canals is simply

$$k_{xx} = \frac{\phi_{\text{fluid}}}{\rho^f \omega} \left[\frac{2 I_1(i^{1/2}\kappa)}{\kappa I_0(i^{1/2}\kappa)} - i \right] \quad (24)$$

In the preceding equations, I_0 and I_1 are the modified Kelvin functions described, for example, in Abramowitz and Stegun [37]. In general, (24) indicates that the effective permeability under oscillatory flow is a complex quantity. However, for relatively low frequencies with $\kappa \ll 1$, the effective permeability in the canal direction tends toward a real value $k_{xx} = \phi_{\text{fluid}} R^2 / 8\mu$. This recovers the well-known Scheidegger result valid when flow in the canals is Poiseuille [38]. In the analysis that follows, the Haversian canals are assumed to be aligned with the X_3 axis of the material coordinate system such that $k_{33} = k_{xx}$. The effective permeabilities in transverse directions (k_{11}, k_{22}) are determined primarily by Volksmann canals and typically have about one tenth the magnitude of that in the longitudinal direction.

Poroelectric Modeling of Haversian Bone

Poroelectric Finite Element Model (Time Domain). At the bone specimen scale ($\ell/\lambda \gg 1$), Haversian bone can be modeled as an anisotropic poroelectric medium, with properties as described above. Accordingly, the dynamic equilibrium of the bulk porous medium (both the bone matrix and Haversian fluid) and that of the fluid relative to the rest of the medium are expressed, respectively as:

$$\bar{\sigma}_{ij,j} + \rho b_j - \rho \ddot{u}_j - \rho^f \ddot{w}_j = 0 \quad (25)$$

$$-\bar{p}^f_{,j} + \rho^f b_j - R_{ji} \dot{w}_i - \rho^f \ddot{u}_j - \frac{\rho^f}{\phi_{\text{fluid}}} \ddot{w}_j = 0 \quad (26)$$

where the range of indices i and j is 1,2,3, and for generality, body forces per unit mass \mathbf{b} have been included. In (25) and (26), expressions of the form $(*)_{,i}$ are shorthand for $\partial(*)/\partial Y_i$ and are thus spatial derivatives on the bone specimen length scale. Also, in (26) the operator denoted R_{ji} is the resistivity tensor of the medium that is simply the matrix inverse of the permeability tensor used in (20).

To facilitate structural analysis for Haversian bone, the macroscopic continuum equations expressed above can be re-cast in a matrix form suitable for finite element implementation. There are a number of possible numerical implementations of the preceding coupled fluid-solid equations of motion. Here a displacement implementation is utilized in which the basic unknowns at each nodal point in the continuum will be three components of solid displacements, and three components of fluid displacement, relative to the solid. Hence there are six unknowns, or degrees of freedom at each node.

$$\mathbf{d}_A = [\bar{u}_1 \quad \bar{u}_2 \quad \bar{u}_3 \quad w_1 \quad w_2 \quad w_3] \quad (27)$$

Accordingly, the matrix equations of motion for all degrees of freedom associated with the A^{th} node in the mesh can be written as follows:

$$\mathbf{M}^{AB} \cdot \ddot{\mathbf{d}}_B + \mathbf{D}^{AB} \cdot \dot{\mathbf{d}}_B + \mathbf{K}^{AB} \cdot \mathbf{d}_B = \mathbf{f}_A^{\text{ext}} \quad (28)$$

Specific expressions for the different matrix operators are as follows

$$\mathbf{M}_{\text{im}}^{AB} = \begin{bmatrix} \int N^A \rho N^B \delta_{\text{im}} d\Omega & \int N^A \rho^f N^B \delta_{\text{im}} d\Omega \\ \int N^A \rho^f N^B \delta_{\text{im}} d\Omega & \int \frac{1}{\phi_{\text{fluid}}} N^A \rho^f N^B \delta_{\text{im}} d\Omega \end{bmatrix} \quad (29a)$$

$$\mathbf{D}_{\text{im}}^{AB} = \begin{bmatrix} 0 & 0 \\ 0 & \int N^A R_{\text{im}} N^B d\Omega \end{bmatrix} \quad (29b)$$

$$\mathbf{K}_{\text{im}}^{AB} = \begin{bmatrix} \int B_{ji}^A C_{jkl} B_{km}^B d\Omega & - \int B_{ji}^A G_j N_{,m}^B d\Omega \\ - \int N_{,i}^A G_i B_{lm}^B d\Omega & \int N_{,i}^A Z N_{,m}^B d\Omega \end{bmatrix} \quad (29c)$$

$$\mathbf{f}_i^{\text{Aext}} = \begin{bmatrix} \int N^A n_j \bar{\sigma}_{ji} d\Gamma + \int N^A \rho b_i d\Omega \\ \int -N^A n_i \bar{p}^f d\Gamma + \int N^A \rho^f b_i d\Omega \end{bmatrix} \quad (29d)$$

In the preceding expressions, N^A denotes the shape function associated with the A^{th} node in the mesh; \mathbf{B}^A is the strain-displacement operator associated with the A^{th} node; δ_{im} is the Kronecker delta function; and $N_{,i}^A$ denotes the spatial derivative of N^A with respect to the i^{th} macroscopic coordinate variable. Further details on the derivation of these equations, and the meaning of the individual terms can be found in Stewart [39].

Frequency Domain Poroelectric Analysis. Under steady state harmonic loadings applied to bone specimens, the total and relative displacement fields in the bone can be represented as the real parts of a complex harmonic oscillating field as follows:

$$\bar{\mathbf{u}}(\mathbf{Y}, t) = \Re\{[\bar{\mathbf{u}}^r(\mathbf{Y}) + i\bar{\mathbf{u}}^i(\mathbf{Y})] \exp(i\omega t)\} \quad (30a)$$

$$\mathbf{w}(\mathbf{Y}, t) = \Re\{[\mathbf{w}^r(\mathbf{Y}) + i\mathbf{w}^i(\mathbf{Y})] \exp(i\omega t)\} \quad (30b)$$

Above $\Re\{\}$ denotes the real part of a complex variable. An alternative polar decomposition representation of the real part of complex fields is as follows:

$$\bar{u}_k(\mathbf{Y}, t) = |\bar{u}_k(\mathbf{Y})| \cos(\omega t + \theta_k) \quad (31a)$$

$$w_k(\mathbf{Y}, t) = |w_k(\mathbf{Y})| \cos(\omega t + \theta_k^f) \quad (31b)$$

where the amplitudes of matrix displacement and relative fluid displacement at a point \mathbf{Y} are $|\bar{u}_k(\mathbf{Y})|$ and $|w_k(\mathbf{Y})|$, and the phase angles of the displacements with respect to the applied harmonic loading are θ_k and θ_k^f .

With the assumption of a complex displacement field, each of the six nodal unknowns in Eq. (28) can be represented as complex variable. Under harmonic loading of a bone specimen, the dynamic steady state matrix equation becomes, in analogy to Eq. (28),

$$[-\omega^2 \mathbf{M} + i\omega \mathbf{D} + \mathbf{K}] \cdot \mathbf{d} = \mathbf{f}^{\text{ext}} \quad (32)$$

Thus under harmonic loading applied to the specimen at a frequency ω , the steady state response of the medium is obtained by solving Eq. (32).

In the complex poroelectric bone model, a complex displacement field gives rise to complex stress and strain fields in the bone. The peak value of stored energy in the poroelectric bone model during steady state oscillations is simply the strain energy in the medium associated with total stresses and strains that are acting in phase with each other:

$$U_s = \int_{\Omega_s} \frac{1}{4} \bar{\sigma}_k \bar{\epsilon}_k [1 + \cos(\theta_k^{\bar{\sigma}} - \theta_k^{\bar{\epsilon}})] d\Omega_s \quad (33)$$

where $\bar{\sigma}_k$ and $\bar{\epsilon}_k$ denote, respectively, the absolute values of the k^{th} stress and strain components at a point \mathbf{Y} , while $\theta_k^{\bar{\sigma}}$ and $\theta_k^{\bar{\epsilon}}$ are their respective phase angles. Conversely, the total energy dissipated in the poroelastic bone model per cycle U_d is the irreversible work done by drag forces in the bone matrix against the flowing vascular fluid. For the complete model, this is computed as follows:

$$U_d = (\pi\omega)^2 \int_{\Omega_s} w_k R_{kj} w_j d\Omega_s \quad (34)$$

In viscoelasticity theory the quantity $\tan \delta$ is a useful indicator of the energy dissipated per radian, normalized by the peak energy stored per cycle [40]. Using the quantities defined in (33) and (34), $\tan \delta$ is easily computed from its definition

$$\tan \delta = \frac{U_d}{2\pi U_s} \quad (35)$$

Peak Fluid Pressures and Shear Stresses. Since it has been postulated that bone cells might be responding to fluid pressure or fluid shear stresses when positive bone adaptation occurs in conjunction with a specific loading program, it is useful to compute both peak fluid pressures and peak fluid shear-stresses from bone poroelasticity models. Under harmonic loading, the fluid pressure at any point $\mathbf{Y} \in \Omega_B$ will be a complex quantity given simply by Eq. (24) when all strains and ζ are complex. The absolute magnitude of the complex pressure at \mathbf{Y} is the peak macroscopic fluid pressure at that point, and the phase angle of the complex pressure determines the degree to which it is in phase with the applied harmonic loading.

Since the poroelasticity model does not directly provide fluid shear stresses, they must be computed from drag-forces between the vascular fluid and the Haversian canal walls. In particular, the drag forces per unit volume of the porous medium exerted by the Haversian fluid on the walls of the Haversian canals are given simply by:

$$\mathbf{F}_{\text{drag}} = \mathbf{R} \cdot \dot{\mathbf{w}} \quad (36)$$

The drag forces per unit volume are created by cumulative shear stresses acting in the Haversian canals, for a fixed volume of cortical bone. Taking into account both the size and volume fraction of the channels that blood flows in, the average wall shear stress in the Haversian canals at a given time and macroscopic location \mathbf{Y} is given by the relation:

$$\tau(\mathbf{Y}) = \frac{\|\mathbf{R} \cdot \dot{\mathbf{w}}\| R_0}{2\varphi_{\text{fluid}}} \quad (37)$$

where R_0 is the radius of the Haversian canals, \mathbf{R} is the medium's resistivity tensor and the inverse of the permeability tensor \mathbf{k} , and φ_{fluid} the associated volume fraction of the Haversian canals. Under steady-state harmonic loading where complex analysis is performed, this shear stress will typically be complex, indicating both its magnitude and phase angle with respect to the excitation. Above, the absolute magnitude of this shear stress is taken.

Results of Poroelastic Computations

Material Properties. In healthy human cortical bone, the Haversian porosity typically falls in the range of 1-5%, and the typical Haversian canals have diameters ranging from 10-70 μm [30]. In this study, two different assumptions are made regarding the bone matrix stiffness and Haversian porosity. In assumption A, the collagen-hydroxapatite bone matrix is assumed to have a Young's modulus of 11 GPa and a Poisson's ratio of 0.39, while the Haversian porosity is assumed to be 1%, and the mean diameter of Haversian canals is assumed to be 20 μm . In assumption B, the bone matrix is assumed to have a Young's modulus of 12 GPa, a Poisson's ratio of 0.38, a Haversian porosity of 4%, and a mean diameter of the Haversian canals of 50 μm . All of these

Table 1 Computed effective poroelastic moduli for Haversian bone with material assumptions A and B. All poroelastic moduli not specified have vanishing values.

Material Assumption A		
$E_{\text{bonematrix}} = 11 \text{ GPa}; \nu_{\text{bonematrix}} = 0.39; \phi_{\text{voids}} = 0.01$		
Undrained Poroelastic Moduli in GPa (Orthotropic)		
$C_{11} = C_{22} = 17.33;$	$C_{12} = C_{21} = 10.30;$	$C_{44} = C_{55} = 4.016;$
$C_{33} = 19.02;$	$C_{23} = C_{32} = 10.65;$	$C_{66} = 3.922;$
	$C_{13} = C_{31} = 10.65;$	
Pore-Pressure Coupling Coefficients in GPa		
$G_1 = G_2 = -6.252;$	$G_3 = -5.164;$	
Storage Modulus in GPa		
$Z = 17.21;$		
Material Assumption B		
$E_{\text{bonematrix}} = 12 \text{ GPa}; \nu_{\text{bonematrix}} = 0.38; \phi_{\text{voids}} = 0.04$		
Undrained Poroelastic Moduli in GPa (Orthotropic)		
$C_{11} = C_{22} = 20.06;$	$C_{12} = C_{21} = 12.13;$	$C_{44} = C_{55} = 4.016;$
$C_{33} = 20.92;$	$C_{23} = C_{32} = 12.30;$	$C_{66} = 3.922;$
	$C_{13} = C_{31} = 12.30;$	
Pore-Pressure Coupling Coefficients in GPa		
$G_1 = G_2 = -6.618;$	$G_3 = -5.390;$	
Storage Modulus in GPa		
$Z = 30.63;$		

values are consistent with the range of accepted values typically reported in the literature [29]. The *in vivo* fluid phase in Haversian bone is blood, whereas that in related experimental studies by Garner et al. [41] and Buechner et al. [42] we model (Section 5) saline which has a bulk modulus of 2.1 GPa, a vanishing shear modulus, and a shear viscosity equal to that of water at 20 °C or approximately $10^{-3} \text{ Pa}\cdot\text{s}$. The effective poroelastic coefficients and permeability coefficients for assumed material properties A and B are presented below.

Using the unit cell finite element analysis model (Fig. 2b), the effective poroelastic moduli (in units of GPa) of the model in (13) have been computed (Table 1). Here, the longitudinal direction of the Haversian canals is taken as aligned with the X_3 coordinate axis. The modeled effective poroelastic compliance (14) of bone is obtained by inverting the effective stiffness as represented in (13). Specific compliance values associated with the stiffness coefficients in Table 1 are as shown in Table 2.

For material assumption B, the effective moduli of Table 1 indicate that when the saturated Haversian bone model is strained uniaxially in the longitudinal direction in an undrained manner the resulting pore fluid pressure (in GPa) in the Haversian canals is $-5.39\bar{\epsilon}_{33}$. Conversely, under undrained conditions, transverse

Table 2 Computed effective poroelastic compliances for material assumptions A and B. All compliances not specified have vanishing values.

Material Assumption A		
Fully Drained Poroelastic Compliances in GPa^{-1} (Orthotropic)		
$S_{11} = S_{22} = .1062;$	$S_{12} = S_{21} = -.03611;$	$S_{44} = S_{55} = .2810;$
$S_{33} = .09261;$	$S_{23} = S_{32} = -.03520;$	$S_{66} = .3042;$
	$S_{13} = S_{31} = -.03520;$	
Pore-Pressure Coupling Coefficients in GPa^{-1}		
$B_1 = B_2 = .001489;$	$B_3 = .002213;$	
Storage Compliance in GPa^{-1}		
$A = .006957;$		
Material Assumption B		
Fully Drained Poroelastic Compliances in GPa^{-1} (Orthotropic)		
$S_{11} = S_{22} = .09262;$	$S_{12} = S_{21} = -.03349;$	$S_{44} = S_{55} = .2490;$
$S_{33} = .08683;$	$S_{23} = S_{32} = -.03297;$	$S_{66} = .2550;$
	$S_{13} = S_{31} = -.03297;$	
Pore-Pressure Coupling Coefficients in GPa^{-1}		
$B_1 = B_2 = .006974;$	$B_3 = .001034;$	
Storage Compliance in GPa^{-1}		
$A = .003584;$		

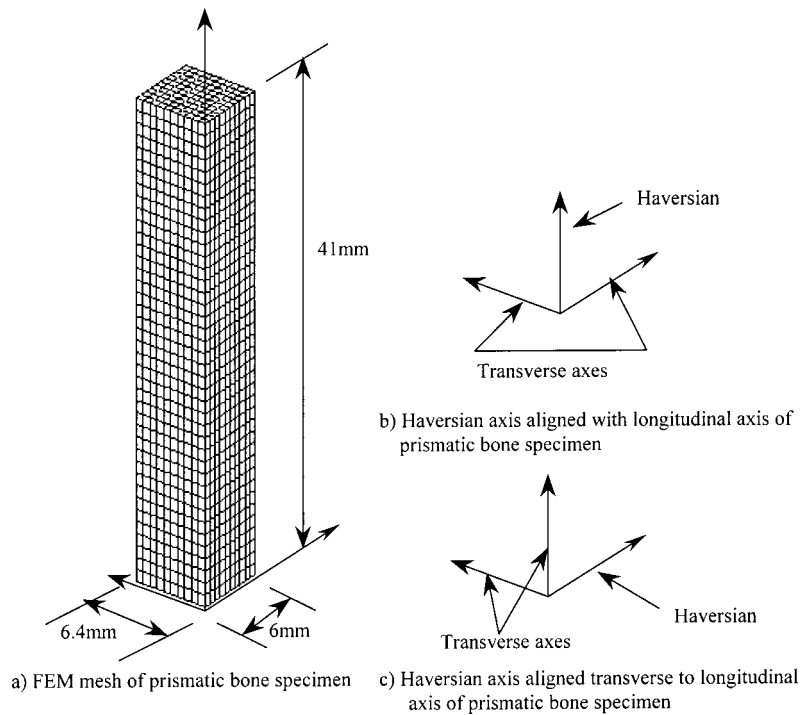


Fig. 3 a) Finite element model of prismatic cortical bone specimen; b) Haversian canals oriented in alignment with longitudinal axis of specimen; c) Haversian canals oriented transverse to longitudinal axis of bone specimen.

uniaxial strain gives a pore fluid pressure of $-6.62(\bar{\epsilon}_{11}$ or $\bar{\epsilon}_{22})$. Pure shear strains in any of the coordinate planes do not give rise to any pore fluid pressure.

When a transverse uniaxial compressive stress $\bar{\sigma}_{11}$ or $\bar{\sigma}_{22}$ is applied to the model (material assumption B), the change in fluid content necessary (per unit applied stress) to relieve fluid pressure is $B_1 = B_2 = .006974 \text{ GPa}^{-1}$. Alternatively, for compressive stresses applied in the longitudinal direction $\bar{\sigma}_{33}$, the reduction in fluid content required to relieve the fluid pressure is $B_3 = .001034 \text{ GPa}^{-1} \bar{\sigma}_{33}$. Thus, the model predicts that transverse stresses applied to Haversian bone have the potential to generate significantly stronger flows in the Haversian system than do stresses applied longitudinally.

For material assumption B, the inverted compliances $S_{11}^{-1} = S_{22}^{-1}$ of the model yield a fully drained Young's modulus of bone in the transverse direction of 10.8 GPa. In the direction aligned with the Haversian canals $S_{33}^{-1} = 11.57 \text{ GPa}$. Since the nominal value of the bone matrix Young's modulus associated with material assumption B is 12 GPa, it is seen that Haversian canals with a 4% volume fraction produce larger reduction in transverse Young's modulus than in the longitudinal Young's modulus. This result is consistent with results that would be produced by other micro-mechanical analysis techniques for composite and/or heterogeneous materials.

Under the assumption of Poiseuille flow, the absolute hydraulic conductivity in the direction of the Haversian canals would be, in accordance with Scheidegger's result, approximately $1.25 \cdot 10^{-13} \text{ m}^2$ for material assumption A and approximately $3.0 \cdot 10^{-12} \text{ m}^2$ for material assumption B. In transverse directions, the estimated permeability would be about one tenth that in the longitudinal direction, due to Volkmann canals and also randomly oriented canaliculi. These estimates are actually in quite good agreement with the measured conductivities of human cortical bone reported by Rouhana et al. [43] which ranged from $1.5 \cdot 10^{-13} \text{ m}^2$ to $5.7 \cdot 10^{-13} \text{ m}^2$ in the longitudinal direction, and from $1.3 \cdot 10^{-14} \text{ m}^2$ to $5.5 \cdot 10^{-14} \text{ m}^2$ in the transverse directions.

Time Domain Fluid Pressure Relaxation Behaviors. When an external mechanical load is applied very rapidly to saturated Haversian bone, both the solid bone matrix and the Haversian fluid initially share the load and thus contribute to the overall stiffness of the medium. If the boundaries of the bone specimen permit drainage, the fluid will flow toward the draining boundaries, resulting in the dissipation of fluid pressure in the Haversian lumens. As this occurs, the Haversian lumens contract, resulting in a slight stiffness reduction of the bone. Also, as the fluid flows to the boundaries, the work done by viscous drag forces between the fluid and solid phases results in dissipation of mechanical energy. The related phenomena of stiffness relaxation and energy dissipation associated with fluid flow contribute to the apparent viscoelastic behavior of Haversian bone. Of course, fluid flow in Haversian canals is only one of a number of dissipative viscoelastic mechanisms in bone. Others include the inherent viscoelasticity of the cement-line material between osteons, molecular motions in collagen, and fluid flow both in the canalicular-lacunar system and within the nano-pores of the hydroxapatite bone matrix.

In the experimental study reported by Garner et al. [41], cylindrical bone specimens (3mm by 17mm) harvested from the cortical region of a human cadaver's femur were completely restrained on their lower surface. The physical bone specimens were saturated with water, and then subjected to dynamic bending and torsion tests over a wide range of frequencies. Continuous bending moment versus curvature measurements and continuous torque versus twist angle measurements were recorded and used to compute total rates of energy dissipation in the bone specimen. The response of the cortical bone was measured both when the Haversian canals (and thus the direction of greatest permeability) were aligned with the long axis of the cylinder, and also when the Haversian canals were transverse to the longitudinal axis of the cylinder. Similar experiments were also performed and reported by Buechner et al. [42] on rectangular prismatic bovine bone specimens where size effects were investigated.

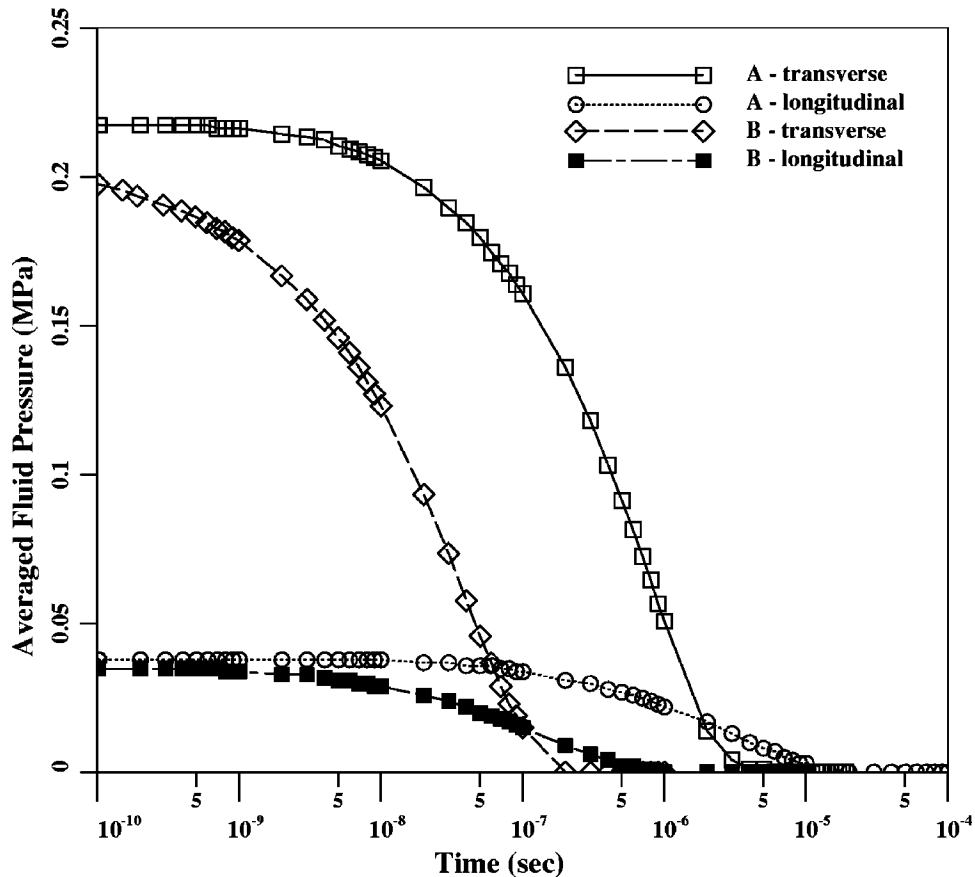


Fig. 4 Computed fluid pressure relaxation responses in the model of cortical bone specimens for both sets of poroelastic properties, and for both longitudinal and transverse orientation of the Haversian canals. A uniaxial stress of 1 MPa was applied to the bone model. When the Haversian canals are oriented longitudinally in the prismatic bone specimen, initial fluid pressures are smaller but pressure relaxation takes longer.

A numerical model (Fig. 3a) of the rectangular prismatic specimens was created by discretizing a parallelepiped (6mm by 6.4mm by 41mm) into a mesh of hexahedral trilinear poroelastic finite elements (40 layers of elements with 100 elements per layer). In this bone-specimen model, both a longitudinal and transverse orientation of the Haversian canals were considered as shown in Figs. 3b and 3c. This numerical model was employed first to compute the consolidation response of the cortical bone to a step function loading of 1 MPa in order to note the characteristic times required for the fluid pressure to decay. The same model was subsequently used to compute steady-state dynamic bending responses of poroelastic bone over a wide range of frequencies. In the dynamic bone-specimen computations, a rotation was applied to the free end of the prismatic bone specimen at prescribed frequencies, and for each frequency, the steady state response of the bone-specimen was computed.

For both material assumptions A and B the consolidation behavior of the rectangular, prismatic specimen described above was computed. The computed volume-averaged pore fluid pressures have been plotted versus time with both the longitudinal and transverse orientations of Haversian canals in the prismatic specimen (Fig. 4). Inertial effects were neglected in these pressure relaxation computations, and the uniformly applied surface traction remained constant for the duration of the test. When initially applied, the surface traction is supported by both the solid and fluid phases within the bone. The behavior of the bone immediately after the load is applied represents the undrained, short-term response of the material. When loaded respectively in the longitudinal and transverse directions, the undrained pore fluid under

material assumption A experiences pressures with relative magnitudes of 4.5% and 22% in relation to the applied axial stress on the bone specimen. Under material assumption B, the peak pressures under longitudinal and transverse loadings are again, respectively, about 4.5% and 20% of the applied stress magnitude. When the load is first applied to the bone specimen, there is an essentially a state of uniform uniaxial stress in the bone model, and the associated fluid pressures can be found directly from the linear poroelastic models of Eqs. (13) and (14) and the material properties found from unit cell analysis (Tables 1 and 2). These results make it clear that uniaxial stress loadings in directions orthogonal to the Haversian canals have the potential to generate larger Haversian fluid pressures and stronger load-induced flows.

For the material assumptions invoked in the computational models, and for the assumed specimen size, the computed Haversian fluid pressure relaxation times range from approximately 10^{-8} seconds to 10^{-5} seconds. These relaxation times are generally consistent with the relaxation times of order 10^{-6} seconds estimated by Zhang et al. [27].

Results of Harmonic Loading Computations. The peak fluid pressures (Fig. 5) and peak fluid shear stresses (Fig. 6) in the bone model were computed with each frequency (Fig. 5). At each frequency considered, the peak bone bending pressure $\Omega_B^{\max}[-1/3(\bar{\sigma}_{11} + \bar{\sigma}_{22} + \bar{\sigma}_{33})]$ was used to normalize the peak bone fluid pressure, and the peak fluid shear stress at that frequency. The computed results (Fig. 5) indicate that the ratio of peak fluid pressures to peak bone pressures start out very small [$O(10^{-7} - 10^{-5})$] at 1 Hz and increase linearly with frequency

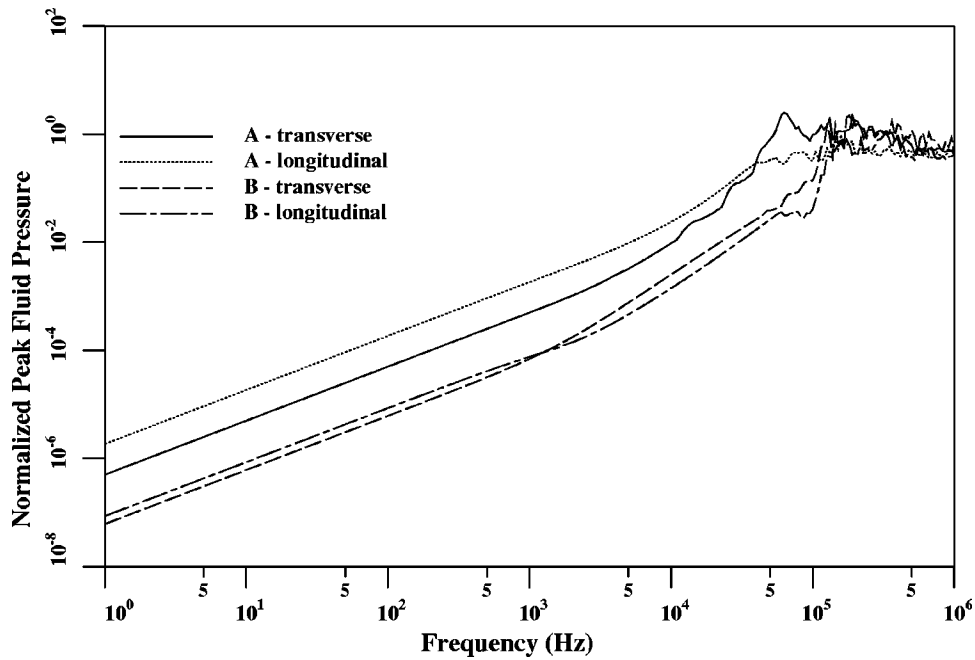


Fig. 5 Computed peak Haversian fluid pressures versus frequency for material assumptions A and B, and both transverse and longitudinal orientation of the osteonal bone in the prismatic specimen model. At each frequency, the computed fluid pressures have been normalized by the peak bone pressure in the corresponding model at that same frequency.

through approximately 10 kHz. Beyond 100 kHz the ratio of peak fluid pressures to peak bone pressures are consistent with what would be seen in the fully undrained behavior of cortical bone. While the pressure relaxation results of Fig. 4 indicate that fully undrained behavior occurs only above 1 MHz, it is postulated here that breakdown of Poiseuille flow leads to “undrained” behavior at “lower” frequencies. Above 100 kHz the computed bone fluid

pressures, under bending with Haversian canals oriented transversely to the long axis of the prismatic specimen, are consistently larger than fluid pressures under longitudinal orientation of the Haversian canals. Conversely, at lower frequencies, loading of the bone in the direction of the Haversian canals generates larger Haversian fluid pressures, presumably because of the larger fluid drainage distances and relaxation times in the long direction of the

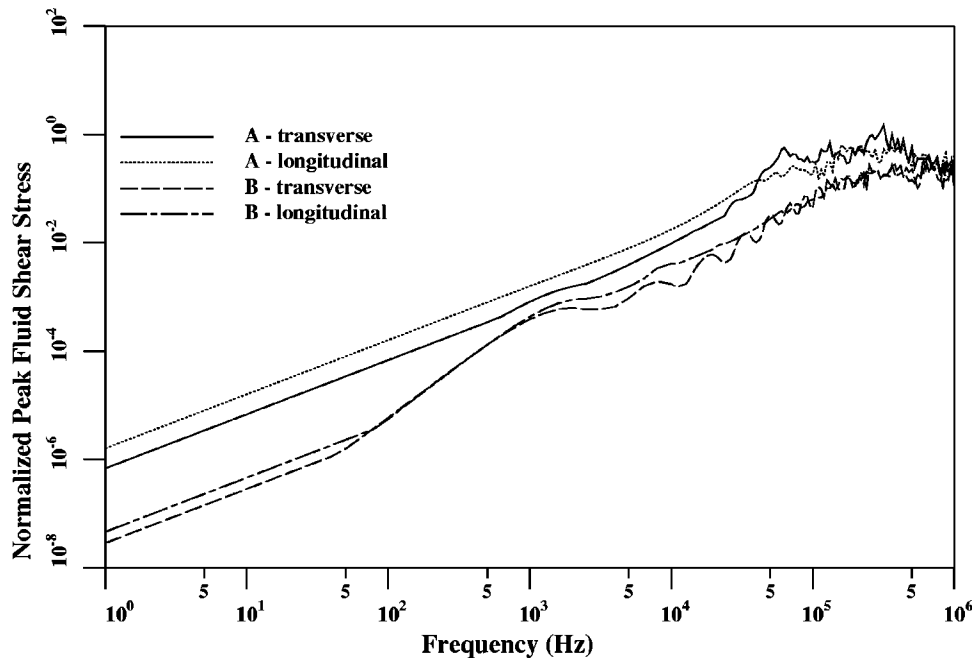


Fig. 6 Computed peak Haversian shear stresses versus frequency for material assumptions A and B, and both transverse and longitudinal orientation of the osteonal bone in the prismatic specimen model. At each frequency, the computed fluid shear stresses have been normalized by the peak bone pressure in the corresponding model at that same frequency.

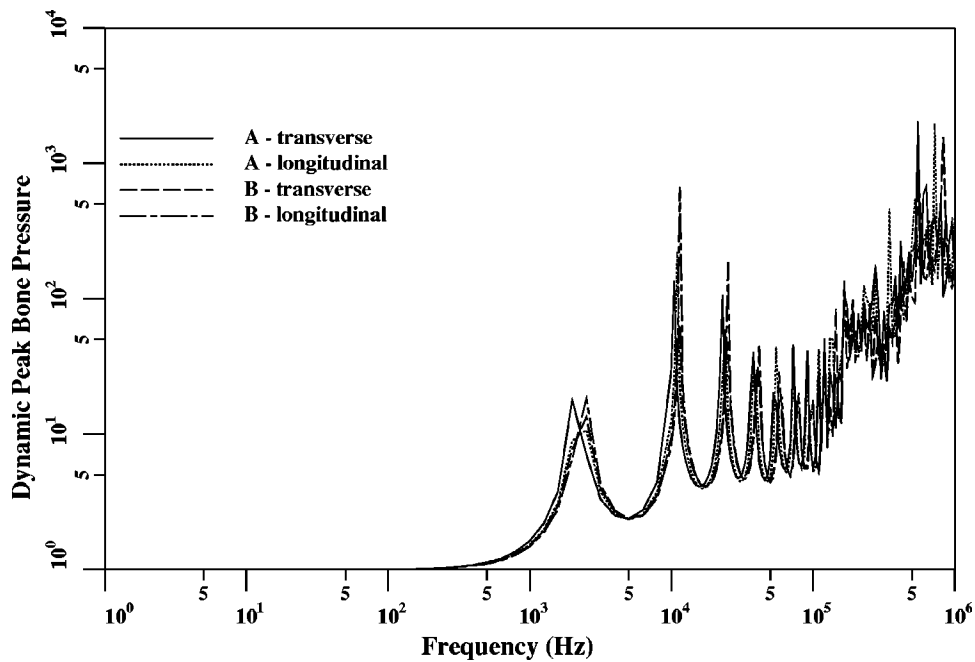


Fig. 7 Computed peak bone pressures versus frequency for material assumptions A and B, and both longitudinal and transverse orientation of osteonal bone within the prismatic specimen model. For each model, the computed dynamic peak bone pressures have been normalized by the static peak bone pressure for that same model.

bone specimens. Peak Haversian fluid shear stresses (Fig. 6) increase linearly in proportion to both the excitation frequency and the load magnitude up to a frequency of 100 Hz for material assumption B, and up to a frequency of 10 kHz for material assumption A.

In the experimental study of Garner et al. [41], saturated human cortical bone specimens described therein were subjected to a series of harmonic bending and torsional loadings to measure the rates of energy dissipation. In particular, $\tan \delta$ values were reported based on the measurements. Both water-saturated specimens, and moist, non-saturated specimens were tested, with differences in their responses being attributed, at least in part, to load-induced fluid flow effects in the saturated bone specimens. Statistically significant differences in $\tan \delta$ characteristics between the moist and saturated bone specimens, if they were apparent, could provide indirect confirmation of load-induced fluid flow in bone, which is hard to confirm directly.

The computed $\tan \delta$ versus frequency responses of the bone specimens with material assumptions A and B for both longitudinal and transverse orientations of the Haversian canals compared to experimentally measured values reported by Garner et al. [41] (Fig. 8). As expected, the computed $\tan \delta$ values are substantially larger at frequencies above 1 kHz than below, with $\tan \delta$ values under transverse orientation of the Haversian canals larger than those under longitudinal orientation. The computed response of the prismatic bone specimens is essentially quasi-static up to the first resonant frequency at approximately 1 kHz, and beyond this, the bone model experienced numerous different resonance modes as shown by the spikes in normalized bending stresses (Fig. 7). The computed values of $\tan \delta$ (Fig. 8) are clearly much smaller than those measured experimentally by Garner et al.

Discussion of Methods and Results

The model results of the preceding section indicate that bone fluids in the Haversian system flow quite freely at physiologically meaningful frequencies (1-100 Hz) making it difficult to build up large load-induced fluid pressures in the Haversian system at such frequencies. Nevertheless, very moderate load-induced pressures

can be generated at physiological frequencies. For example, to generate excess Haversian bone fluid pressures of 1 Pa at 1 Hz, a loading of approximately 10 MPa would be required, while at 100 Hz, a loading of only approximately 0.10 MPa would be required.

In the quasi-static range of responses, the modeled peak fluid shear stresses in the Haversian canals increase linearly with the magnitude of loading applied to the bone, and also linearly with the frequency of the excitation. Recent *in vitro* experiments by Jacobs et al. [26] have shown that chick osteocytes respond to oscillatory fluid shear stresses of 2 Pa, resulting in alterations of intracellular calcium concentrations (possibly related to remodeling responses). These responses are at least consistent with the notion that osteocytes could be sensing cells which then somehow communicate the mechanical environment to responding cells (e.g. osteoblasts). Shear stresses of similar magnitude in the Haversian fluid can be achieved in the proposed bone poroelasticity models a number of possible ways by varying both the magnitude and loading of the applied excitation. Using the results and constants of proportionality indicated by Fig. 6, shear stresses of 2 Pa could be achieved by applying bending excitation with a peak bending stress of 10 MPa at a frequency of 1 Hz, a peak bending stress of 1 MPa at a frequency of 10 Hz, or even a bending stress of 0.1 MPa at a frequency of 100 Hz.

These model-based observations are premised on the notion that the Haversian canals are devoid of soft tissue and have semi-rigid boundaries. The micrographic study by Cooper indicates that these assumptions are not strictly true since soft tissues fill at least a substantial portion of the lacunae and Haversian canals [30]. To what extent these tissues would impair fluid flow is unknown. It is worth noting that based on *in vitro* permeability experiments on fresh cortical bone reported by Rouhana et al. [43], fresh bone specimens had absolute permeabilities of order $10^{-13} - 10^{-15} \text{ m}^2$. However, over many days of water flowing through the bone specimens, the permeabilities gradually increased until they reached final values approximately one to two orders of magnitude larger ($10^{-11} - 10^{-13} \text{ m}^2$). It is indeed conceivable that the initial lower permeabilities are indicative of the *in vivo* perme-

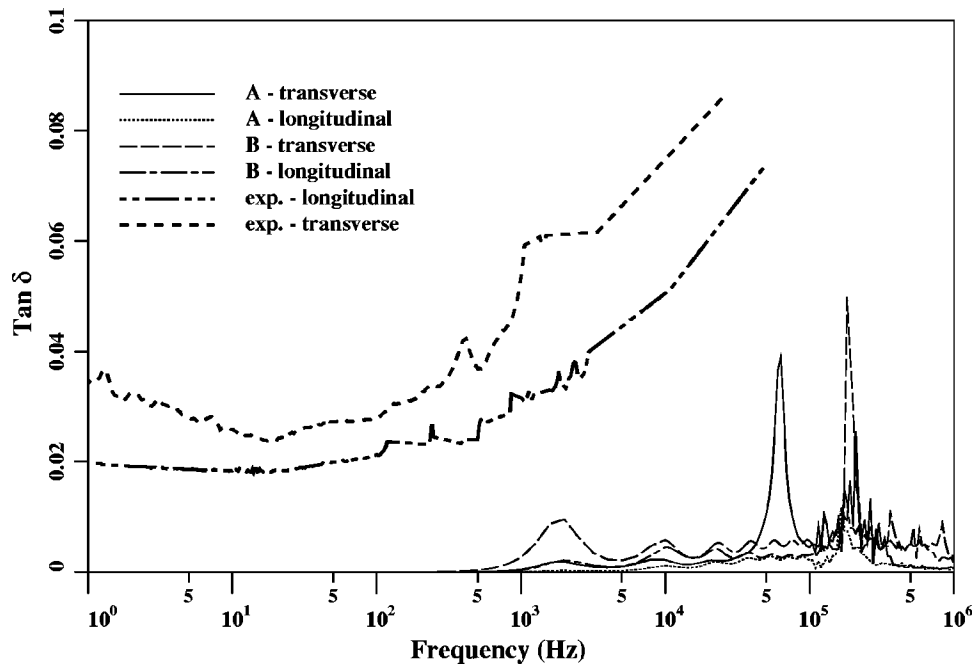


Fig. 8 Computed $\tan \delta$ versus frequency for material assumptions A and B, and both longitudinal and transverse orientation of osteonal bone within the prismatic specimen model. The computed values are compared with experimentally measured $\tan \delta$ by Garner et al. (2000).

abilities associated with Haversian bone, and that the later permeabilities are indicative of those that occur only when all of the soft tissues have been washed out of the Haversian canals. On the other hand, when bone specimens are cut by saw for experiments, a good deal of the bone architecture in the vicinity of the cut can be disturbed, and residue from the cutting can possibly clog Haversian canals, leading to unrealistically low fluid conductivity measurements until the residue from cutting the bone has been flushed out.

If we had, in this effort, modeled the Haversian canals as being partially filled with soft tissues, the frequencies at which peaks in $\tan \delta$ and also peaks in fluid pressure occur could be as much as two orders of magnitude smaller than computed herein. It is further acknowledged that if the model were to account for partial filling of the Haversian canals with soft tissue, the computed $\tan \delta$ values could also be modified significantly.

Osteons tend to spiral about the long axis of bones [44–48], although they are far more aligned with the long [46] than transverse axis even in those bones where this feature is prominent and well documented (e.g., the femur). Furthermore, the notion of spiraling of osteons is controversial, and some authors have found no such effects [49,50]. In any case, such spiraling would not likely have a major effect because the alignment differences would be no more than 5–15 degrees. Any resulting changes to our model results would lie between those for the longitudinal and transverse orientations of the Haversian canals, but closer to the former. Were the effects of spiraling osteons important to ascertain such effects could certainly be modeled at the whole-bone scale.

In general, the branches of osteons are aligned closely to the long axis of the bone, and as with the spiraling of osteons, would not likely have much effect as a result of orientation alone. They would, however, have the tendency to promote what we have termed transverse “drainage” or flow in the bone. [In fact, this is the reason for our use of a transverse permeability roughly one tenth that in the longitudinal direction.] Given that branching appears to involve a relatively small (perhaps less than 5–10%) of the length of the osteon [44], we suspect the gross effect on stress gradients and flow would be of that same order.

Since the numerical model presented is mathematically linear,

the magnitude of computed peak fluid pressures and shear stresses at a given excitation frequency will always be in proportion to the magnitude of loading applied to a given specimen model. In Figs. 5 and 6, we have for each frequency normalized both the peak fluid pressure and the peak fluid shear stress in the specimen model by the peak mean normal stress in the model at that frequency. Since many of the loading frequencies considered were well above the fundamental frequency of the bone-specimen model, the computed responses were highly dynamic in that inertial forces within the specimen were very significant if not dominant. In the highly dynamic range the structural (as opposed to material) stiffness characteristics of the bone specimen model are strongly frequency dependent and as a result the fluid pressures and fluid shear stresses induced in the bone model will depend upon the mass and stiffness characteristics of the specimen being considered.

As it is very difficult to measure fluid flow, and fluid stresses on the microscale of small bone specimens undergoing dynamic loading, these quantities are not easily verified experimentally. In related experimental work by Garner et al. [41] and Buechner et al. [42], the rate of energy dissipation in the bone at different frequencies of excitation, as manifested by $\tan \delta$, was measured. In the current computations the first calculated peaks in $\tan \delta$ (Fig. 8) occurring below ($f=10^5$ Hz) correspond to peaks in mean bone stress (Fig. 7) associated with resonance of the bone specimen. Only two apparent true peaks in $\tan \delta$ associated with fluid flow are seen in the model results of Fig. 8. The first occurs for material assumption A under transverse loading at $f=70$ kHz, and the second occurs for material assumption B under transverse loading at $f=200$ kHz.

Since the current work deals only with fluid flow in the Haversian system, and the associated energy dissipated therein, it is not necessarily surprising or disturbing that the $\tan \delta$ values computed herein are much smaller than those measured in experimental work. As additional mechanisms are included in the bone poroelasticity models, such as fluid flow in the canaliculi, and in the hydroxapatite matrix pores, it is anticipated that the models will more closely resemble the experimental observations.

It is interesting to note that macroscopically, load-induced fluid flow in the Haversian system of cortical bone has only a negligible effect in terms of the effective viscoelasticity associated with pore pressure relaxation effects. However, bone poroelasticity models can yield potentially useful information on phenomena occurring within the bone during loading. Here, attention has been focused on the fluid pressures and shear stresses generated in the Haversian system during loading of cortical bone. In a following work a hierarchical bone poroelasticity model will be presented and applied to compute representative fluid pressures, shear stresses, and energy dissipation in the lacunar-canalicular system.

Perhaps the most fundamental hypothesis of this work is that fluid flow and associated shear stresses relate in some way to bone adaptation. Alternative explanations include stress-related phenomena arising from the matrix of bone and non-mechanical phenomena arising from genetically-based mechanisms or reactions to hormonal (systemic) [51–54], paracrine [55–59], or autocrine [54–56, 59] functions. While not excluding these sorts of mechanisms, the present work rather assumes based upon considerable theoretical [22–25, 61–65], and experimental [26, 57, 66–74] work that fluid flow and associated shear stresses can contribute to remodeling.

Given potential fluid flow mechanisms, the next fundamental question is at what level do these result in bone adaptation. We presume stress-engendered flow occurs at all levels (e.g., grossly visible inter-trabecular spaces within the marrow, Haversian systems and porosities which may be grossly visible in cut cortical bone, and Haversian, Volkman, or canalicular systems seen only with light or electronic microscopy). Then one must ask whether these are relevant. We focus here upon the systems in cortical bone, but do not exclude the relevance at any level. In fact, the cutting cones of newly-forming Haversian systems contain osteoblasts which might be mechanically sensitive to fluid flow. The present analysis would provide some predictions of fluid flow at this level, while not excluding sensitivity at other levels (e.g., osteocytes embedded in lacunae, or osteocytic processes embedded in canaliculi).

We unfortunately have no way of directly studying the mechanosensitivity of bone cells *in vivo*. Therefore, we are left with comparing our predictions of fluid pressure to that in experiments using isolated cells. We acknowledge isolated cells *in vitro* may respond in vastly differing ways than embedded cells *in vivo*. However, cell culture in general has shown in many sorts of studies (i.e., responses to pharmaceutical and genetic manipulation) to reflect biological responses subsequently shown *in vivo*, and they have been frequently used to explore mechanisms of mechanotransduction. Thus, while not clearly confirming the utility of this model, they are at least consistent with our findings.

Our approach, indeed almost any mechanical model, implicitly excludes biological factors such as systemic or genetic effects. Without a quantitative knowledge (or assumption) of these interactions, we would not know how to include them. Eliminating such factors in modeling clearly has the disadvantage of excluding potentially critical factors, but has the advantage of studying only mechanical effects and ascertaining their potential role. If estimates of fluid flow and shear stresses are either far too low or too high to result in physiological effects, they may be excluded from consideration.

Conclusions

In this work, unit cell analysis has been applied to relate the morphology of Haversian bone to its effective anisotropic poroelastic properties. The anisotropic bone poroelasticity model was then exercised on a cortical bone specimen in the frequency range of 1 Hz to 1 MHz. Drag forces between the Haversian fluid and the bone matrix were quantified in the bone poroelasticity models and then related to fluid shear stresses. This analysis suggests that fluid shear stresses in the Haversian system on the order of 1 Pa are easily achievable in the physiological range (1–100

Hz) with bone stresses in the range of ($10^7 - 10^5$ Pa). If it could be verified that osteocytes do indeed respond to oscillatory fluid shear stresses of this magnitude *in vivo* then the hypothesis that fluid shear stresses on bone cells are an important mechanotransduction mechanism in the phenomenon of bone adaptation would be strengthened.

Acknowledgements

The authors wish to gratefully acknowledge financial support from Whitaker Foundation grant 96-0636 that supported this research.

References

- [1] Burger, E. H., Klein-Nulend, J., van der Plas, A., and Nijweide, P. J., 1995, "Function of Osteocytes in Bone—Their Role in Mechanotransduction," *J. Nutr.*, **125**, pp. 2020S–2023S.
- [2] Cowin, S. C., Moss-Salentijn, L., and Moss, M. L., 1991, "Candidates for the Mechanosensory System in Bone," *J. Biomech. Eng.*, **113**, pp. 191–197.
- [3] Rubin, C. T., and McLeod, K. J., 1994, "Promotion of Bony Ingrowth by Frequency-Specific, Low-Amplitude Mechanical Strain," *Clin. Orthop.*, **298**, pp. 165–174.
- [4] Qin, Y. X., McLeod, K. J., Guilak, F., Chiang, F. P., and Rubin, C. T., 1996, "Correlation of Bony Ingrowth to the Distribution of Stress and Strain Parameters Surrounding a Porous-coated Implant," *J. Orthop. Res.*, **14**, pp. 862–870.
- [5] Wolff, J., 1892, "Das Gesetz der Transformation der Knochen," Verlag von August Hirschwald, Berlin.
- [6] Glücksmann, A., 1939, "Studies on Bone Mechanics In Vitro: II. The Role of Tension and Pressure in Chondrogenesis," *J. Anat.*, **73**, pp. 39–55.
- [7] Frost, H. M., 1966, "Bone as a Physiological Tool," *Henry Ford Hosp. Med. J.*, **14**, pp. 63–70.
- [8] Lanyon, L. E., and Smith, R. N., 1970, "Bone Strain in the Tibia During Normal Quadrupedal Locomotion," *Acta Orthop. Scand.*, **41**, pp. 238–248.
- [9] Chamay, A., and Tschantz, P., 1972, "Mechanical Influences in Bone Remodeling. Experimental Research on Wolff's law," *J. Biomech.*, **5**, pp. 173–180.
- [10] Hassler, C. R., Rybicki, E. F., Cummings, K. D., and Clark, L. C., 1977, "Quantitation of Compressive Stress and its Effects Upon Bone Remodeling [proceedings]," *Bull. Hosp. Jt. Dis.*, **38**, pp. 90–93.
- [11] Lanyon, L. E., and Bourn, S., 1979, "The Influence of Mechanical Function on the Development and Remodeling of the Tibia. An Experimental Study in Sheep," *J. Bone Jt. Surg., Am. Vol.*, **61**, pp. 263–273.
- [12] Frost, H. M., 1982, "Mechanical Determinants of Bone Modeling," *Metab. Bone Dis. Relat. Res.*, **4**, pp. 217–229.
- [13] Lanyon, L. E., Goodship, A. E., Pye, C. J., and MacFie, J. H., 1982, "Mechanically Adaptive Bone Remodeling," *J. Biomech.*, **15**, pp. 141–154.
- [14] Rubin, C. T., and Lanyon, L. E., 1984, "Regulation of Bone Formation by Applied Dynamic Loads," *J. Bone Jt. Surg., Am. Vol.*, **66**, pp. 397–402.
- [15] Carter, D. R., Fyhrie, D. P., and Whalen, R. T., 1987, "Trabecular Bone Density and Loading History: Regulation of Connective Tissue Biology by Mechanical Energy," *J. Biomech.*, **20**, pp. 785–794.
- [16] Yasuda, L., 1954, "On the Piezoelectric Activity of Bone," *J. Jpn Orthop Surg Soc.*, **28**, pp. 267.
- [17] Fukada, E., and Yasuda, L., 1957, "On the Piezoelectric Effect of Bone," *J. Physiol. Soc. Jpn.*, **12**, p. 1158.
- [18] Bassett, C. A. L., and Becker, R. O., 1962, "Generation of Electric Potentials in Bone in Response to Mechanical Stress," *Science*, **137**, pp. 1063–1064.
- [19] Piekarski, K., and Munro, M., 1977, "Transport Mechanism Operating Between Blood Supply and Osteocytes in Long Bones," *Nature (London)*, **269**, pp. 80–82.
- [20] Iannaccone, W., Korostoff, E., and Pollack, S. R., 1979, "Microelectrode Study of Stress-Generated Potentials Obtained from Uniform and Nonuniform Compression of Human Bone," *J. Biomed. Mater. Res.*, **13**, pp. 753–763.
- [21] Starkebaum, W., Pollack, S. R., and Korostoff, E., 1979, "Microelectrode Studies of Stress-Generated Potentials in Four-point Bending of Bone," *J. Biomed. Mater. Res.*, **13**, pp. 729–751.
- [22] Salzstein, R. A., Pollack, S. R., Mak, A. F. T., and Petrov, N., 1987, "Electromechanical Potentials in Cortical Bone—I. A Continuum Approach," *J. Biomech.*, **20-3**, pp. 261–270.
- [23] Salzstein, R. A., and Pollack, S. R., 1987, "Electromechanical Potentials in Cortical Bone—II. Experimental Analysis," *J. Biomech.*, **20-3**, pp. 271–280.
- [24] Weinbaum, S., Cowin, S. C., and Zeng, Y., 1994, "A Model for the Excitation of Osteocytes by Mechanical Loading-Induced Bone Fluid Shear Stresses," *J. Biomech.*, **27**, pp. 339–360.
- [25] Jacobs, C. R., Yellowley, C. E., Davis, B. R., Zhou, Z., Cimbala, J. M., and Donahue, H. J., 1998, "Differential Effect of Steady Versus Oscillating Flow on Bone Cells," *J. Biomech.*, **31**, pp. 969–976.
- [26] Zhang, D., Weinbaum, S., and Cowin, S. C., 1998, "Estimates of the Peak Pressures in Bone Pore Water," *J. Biomech. Eng.*, **120**, pp. 697–703.
- [27] Zhang, D., Weinbaum, S., and Cowin, S. C., 1998, "On the Calculation of Bone Pore Water Pressure Due to Mechanical Loading," *Int. J. Solids Struct.*, **35**, pp. 4981–4997.
- [28] Cooper, R. R., Milgram, J. W., and Robinson, R. A., 1966, "Morphology of the

- Osteon. An Electron Microscopic Study," *J. Bone Jt. Surg., Am. Vol.*, **48**, pp. 1239–1271.
- [29] Biot, M. A., 1941, "General Theory of Three-Dimensional Consolidation," *J. Appl. Phys.*, **12**, pp. 155–164.
- [30] Biot, M. A., 1956, "Theory of Propagation of Elastic Waves in a Fluid-saturated Porous Solid. II. Higher Frequency Range," *J. Acoust. Soc. Am.*, **28-2**, pp. 179–191.
- [31] Biot, M. A., and Willis, D. G., 1957, "The Elastic Coefficients of the Theory of Consolidation," *J. Appl. Mech.*, **24**, pp. 594–601.
- [32] Guedes, J., and Kikuchi, N., 1991, "Preprocessing and Postprocessing for Materials Based on Homogenization Method and Adaptive Finite Element Methods," *Comput. Methods Appl. Mech. Eng.*, **83**, pp. 143–198.
- [33] Suquet, P., 1987, "Elements of Homogenization for Inelastic Solid Mechanics," in *Homogenization Techniques for Composite Media*, Sanchez-Palencia, E., and Zaoui, A. (Eds.), Springer-Verlag, pp. 193–278.
- [34] Swan, C. C., 1994, "Techniques for Stress- and Strain-Controlled Homogenization of Inelastic Periodic Composites," *Comput. Methods Appl. Mech. Eng.*, **117**, pp. 249–267.
- [35] Abramowitz, M., and Stegun, I. E., 1964, *Handbook of Mathematical Functions*, National Bureau of Standards, U.S. Department of Commerce.
- [36] Scheidegger, A. E., 1957, *The Physics of Flow Through Porous Media*, MacMillan, New York.
- [37] Stewart, K. J., 2000, *Deformation Induced Fluid Flow as a Mechanism of Bone Adaptation*, M.S. Thesis, The University of Iowa, Iowa City.
- [38] Ferry, J. D., 1980, *Viscoelastic Properties of Polymers*, Wiley, New York.
- [39] Cowin, S. C., Weinbaum, S., and Zeng, Y., 1995, "A Case for Bone Canalliculi as the Atomical Site of Strain Generated Potentials," *J. Biomech.*, **28**, pp. 1281–1297.
- [40] Garner, E., Lakes, R., Lee, T., Swan, C., and Brand, R., 2000, "Viscoelastic Dissipation in Compact Bone: Implications for Stress-Induced Fluid Flow in Bone," *J. Biomech. Eng.*, **122**, pp. 166–172.
- [41] Buechner, P. M., Lakes, R. S., Swan, C., and Brand, R. A., 2001, "A Broad-band Viscoelastic Spectroscopic Study of Bovine Bone: Implications for Fluid Flow," *Ann. Biomed. Eng.*, **29**, pp. 719–728.
- [42] Rouhana, S. W., Johnson, M. W., Chakkalakal, D. A., Harper, R. A., and Katz, J. L., 1981, "Permeability of Compact Bone," *Joint ASME-ASCE Conference. AMD*, 169–172.
- [43] Cohen, J., and Harris, W. H., 1958, "The Three-Dimensional Anatomy of Haversian Systems," *J. Bone Jt. Surg., Am. Vol.*, **40**, pp. 419–434.
- [44] Baltadzhiev, G., 1994, "Morphology of the Haversian Canal. An Electron Microscopic Study," *Folia Med. (Plovdiv)*, **36**, pp. 21–28.
- [45] Hert, J., Fiala, P., and Petryl, M., 1994, "Osteon Orientation of the Diaphysis of the Long Bones in Man," *Bone (N.Y.)*, **15**, pp. 269–277.
- [46] Petryl, M., Hert, J., and Fiala, P., 1996, "Spatial Organization of the Haversian Bone in Man," *J. Biomech.*, **29**, pp. 161–169.
- [47] Martin, R. B., and Burr, D. B., 1989, *Structure, Function, and Adaptation of Compact Bone*, Raven Press, New York.
- [48] Tappen, N. C., 1982, "The Orientation and Spatial Interrelationships of Osteons in Long Bones," *Anat. Rec.*, **202**, p. 187A.
- [49] Koltze, H., 1951, "Studie sur ausseren Form der Osteone," *Z. Anat. Entwicklungsgesch.*, **115**, pp. 584–596.
- [50] Gaillard, P. J., Herrmann-Erlee, M. P., Hekkelman, J. W., Burger, E. H., and Nijweide, P. J., 1979, "Skeletal Tissue in Culture. Hormonal Regulation of Metabolism and Development," *Clin. Orthop.*, **142**, pp. 196–214.
- [51] Nijweide, P. J., Burger, E. H., and Feyen, J. H., 1986, "Cells of Bone: Proliferation, Differentiation, and Hormonal Regulation," *Physiol. Rev.*, **66**, pp. 855–886.
- [52] Turner, C. H., 1999, "Toward a Mathematical Description of Bone Biology: The Principle of Cellular Accommodation," *Calcif. Tissue Int.*, **65**, pp. 466–471.
- [53] Lanyon, L. E., 1992, "The Success and Failure of the Adaptive Response to Functional Load-bearing in Averting Bone Fracture," *Bone (N.Y.)*, **13**, pp. S17–21.
- [54] Dieudonne, S. C., Semeins, C. M., Goei, S. W., Vukicevic, S., Nulend, J. K., Sampath, T. K., Helder, M., and Burger, E. H., 1994, "Opposite Effects of Osteogenic Protein and Transforming Growth Factor Beta on Chondrogenesis in Cultured Long Bone Rudiments," *J. Bone Miner. Res.*, **9**, pp. 771–780.
- [55] Klein-Nulend, J., Semeins, C. M., Veldhuijzen, J. P., and Burger, E. H., 1993, "Effect of Mechanical Stimulation on the Production of Soluble Bone Factors in Cultured Fetal Mouse Calvariae," *Cell Tissue Res.*, **271**, pp. 513–517.
- [56] Salter, D. M., Wallace, W. H., Robb, J. E., Caldwell, H., and Wright, M. O., 2000, "Human Bone Cell Hyperpolarization Response to Cyclical Mechanical Strain is Mediated by an Interleukin-1 Beta Autocrine/Paracrine Loop [In Process Citation]," *J. Bone Miner. Res.*, **15**, pp. 1746–1755 [MEDLINE record in process].
- [57] Skerry, T. M., 1999, "Identification of Novel Signaling Pathways During Functional Adaptation of the Skeleton to Mechanical Loading: The Role of Glutamate as a Paracrine Signaling Agent in the Skeleton," *J. Bone Miner. Metab.*, **17**, pp. 66–70.
- [58] Sterck, J. G., Klein-Nulend, J., Burger, E. H., and Lips, P., 1996, "1,25-dihydroxyvitamin D3-mediated Transforming Growth Factor-beta Release is Impaired in Cultured Osteoblasts from Patients with Multiple Pituitary Hormone Deficiencies," *J. Bone Miner. Res.*, **11**, pp. 367–376.
- [59] Turner, C. H., 1992, "Functional Determinants of Bone Structure: Beyond Wolff's Law of Bone Transformation [editorial]," *Bone (N.Y.)*, **13**, pp. 403–409.
- [60] Dillaman, R. M., Roer, R. D., and Gay, D. M., 1991, "Fluid Movement in Bone: Theoretical and Empirical," *J. Biomech.*, **24 Suppl 1**, pp. 163–177.
- [61] Zeng, Y., Cowin, S. C., and Weinbaum, S., 1994, "A Fiber Matrix Model for Fluid Flow and Streaming Potentials in the Canaliculi of an Osteon," *Ann. Biomed. Eng.*, **22**, pp. 280–292.
- [62] Turner, C. H., Anne, V., and Pidaparti, R. M., 1997, "A Uniform Strain Criterion for Trabecular Bone Adaptation: Do Continuum-Level Strain Gradients Drive Adaptation?," *J. Biomech.*, **30**, pp. 555–563.
- [63] Srinivasan, S., and Gross, T. S., 2000, "Canalicular Fluid Flow Induced by Bending of a Long Bone," *Med. Eng. Phys.*, **22**, pp. 127–133.
- [64] Cowin, S. C., and Weinbaum, S., 1998, "Strain Amplification in the Bone Mechanosensory System," *Am. J. Med. Sci.*, **316**, pp. 184–188.
- [65] Reich, K. M., Gay, C. V., and Frangos, J. A., 1990, "Fluid Shear Stress as a Mediator of Osteoblast Cyclic Adenosine Monophosphate Production," *J. Cell Physiol.*, **143**, pp. 100–104.
- [66] Klein-Nulend, J., Semeins, C. M., Ajubi, N. E., Nijweide, P. J., and Burger, E. H., 1995, "Pulsating Fluid Flow Increases Nitric Oxide (NO) Synthesis by Osteocytes but Not Periosteal Fibroblasts—Correlation with Prostaglandin Up-regulation," *Biochem. Biophys. Res. Commun.*, **217**, pp. 640–648.
- [67] Hung, C. T., Pollack, S. R., Reilly, T. M., and Brighton, C. T., 1995, "Real-time Calcium Response of Cultured Bone Cells to Fluid Flow," *Clin. Orthop.*, **313**, pp. 256–69.
- [68] Ajubi, N. E., Klein-Nulend, J., Nijweide, P. J., Vrijheid-Lammers, T., Alblas, M. J., and Burger, E. H., 1996, "Pulsating Fluid Flow Increases Prostaglandin Production by Cultured Chicken Osteocytes—a Cytoskeleton-Dependent Process," *Biochem. Biophys. Res. Commun.*, **225**, pp. 62–68.
- [69] Hung, C. T., Allen, F. D., Pollack, S. R., and Brighton, C. T., 1996, "Intracellular Ca²⁺ Stores and Extracellular Ca²⁺ are Required in the Real-Time Ca²⁺ Response of Bone Cells Experiencing Fluid Flow," *J. Biomech.*, **29**, pp. 1411–1417.
- [70] Klein-Nulend, J., Burger, E. H., Semeins, C. M., Raisz, L. G., and Pilbeam, C. C., 1997, "Pulsating Fluid Flow Stimulates Prostaglandin Release and Inducible Prostaglandin G/H Synthase mRNA Expression in Primary Mouse Bone Cells," *J. Bone Miner. Res.*, **12**, pp. 45–51.
- [71] Owan, I., Burr, D. B., Turner, C. H., Qiu, J., Tu, Y., Onyia, J. E., and Duncan, R. L., 1997, "Mechanotransduction in Bone: Osteoblasts are More Responsive to Fluid Forces than Mechanical Strain," *Am. J. Physiol.*, **273**, pp. C810–815.
- [72] Ajubi, N. E., Klein-Nulend, J., Alblas, M. J., Burger, E. H., and Nijweide, P. J., 1999, "Signal Transduction Pathways Involved in Fluid Flow-Induced PGE₂ Production by Cultured Osteocytes," *Am. J. Physiol.*, **276**, pp. E171–178.
- [73] Westbroek, I., Ajubi, N. E., Alblas, M. J., Semeins, C. M., Klein-Nulend, J., Burger, E. H., and Nijweide, P. J., 2000, "Differential Stimulation of Prostaglandin G/H Synthase-2 in Osteocytes and Other Osteogenic Cells by Pulsating Fluid Flow," *Biochem. Biophys. Res. Commun.*, **268**, pp. 414–9.
- [74] Kurokouchi, K., Jacobs, C. R., and Donahue, H. J., 2001, "Oscillating Fluid Flow Inhibits TNF-Alpha-Induced NF-Kappa B Activation via an Ikappa B Kinase Pathway in Osteoblast-Like UMR106 Cells," *J. Biol. Chem.*, **276**, pp. 13499–13504.